Chaos, Solitons and Fractals 180 (2024) 114508

Contents lists available at ScienceDirect

Chaos, Solitons and Fractals

journal homepage: www.elsevier.com/locate/chaos

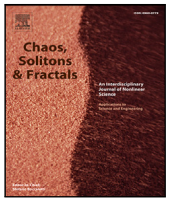

Topological transition between disordered patterns through heating rate-induced defect emergence

Victor Fernandez-Gonzalez [a,*], Sebastián Echeverría-Alar [a], Jorge Vergara [b], Paulina I. Hidalgo [b], Marcel G. Clerc [a]

[a] Departamento de Física and Millennium Institute for Research in Optics, Facultad de Ciencias Físicas y Matemáticas, Universidad de Chile, Casilla 487-3, Santiago, Chile

[b] Departamento de Química Orgánica, Facultad de Ciencias Químicas, Universidad de Concepción, Casilla 160-C, Concepción, Chile

ARTICLE INFO

Keywords:
Topological transitions
Pattern formation
Process dependency
Nonlinear dynamics
Liquid crystals
Chirality

ABSTRACT

Macroscopic systems can exhibit disordered patterns, such as fingerprints, vegetation patterns, and dendrites, which have topological defects that characterize the pattern richness, but their self-organization is unknown. Here, we investigate the formation mechanisms, defect emergence, and topological transition between disordered patterns driven by the heating rate. Based on a thermally driven chiral nematic liquid crystal experiment, we identified the coexistence of two different types of patterns at the same temperature but different heating rates. A supercritical transition is revealed by measuring the density of pattern defects. The pairwise correlation length also suggests this transition. Theoretically, we account for this transition based on an amplitude equation with a chiral term that is valid close to the winding/unwinding transition. Likewise, a prototype model of pattern formation exhibits a similar transition, showing that the transition is universal and could be observed in magnetic, optical, fluid, chemical, and ecological systems.

1. Introduction

Exotic states of matter, including Bose–Einstein condensates, superfluids, chiral magnets, superconductors, and liquid crystalline blue phases, are observed in thermodynamic equilibrium. Rather than being the result of an aggregation of matter (such as the solid, liquid, and gas states), their emergence and characteristic features are due to a change in the topological state of the system [1–4]. The intriguing properties of these exotic states are lost during a topological transition induced by a change in temperature. Likewise, systems that are out of equilibrium through thermal gradients or oscillatory forcing present topological transitions out of equilibrium [5,6]. Hence, depending on the energy injection to which the system is subjected, it may exhibit topological transitions, i.e., the emergence of topological elements or properties in equilibria that were not originally present. These non-equilibrium states are characterized by the self-organization of topological defects. One of the most observed forms of self-organization of topological defects takes place in disordered or turbulent patterns [7–11]. These patterns have a characteristic length but with numerous defects. Fig. 1(d) and (e) shows disordered patterns observed in a chiral nematic liquid crystal cell. Defects can be either local or extended and are topological in nature [12]. The self-organization of defects is responsible for the diversity of patterns in nature, such as those seen in fingerprint patterns [13]. Specifically, defects correspond to phase singularities of the pattern envelope [12,14], as shown in Fig. 2. Indeed, these defects are topologically protected, indicating they possess charges, as evidenced by a discrete jump in the pattern envelope phase. Only defects with opposite charges can be annihilated [10]. These topological defects persist as long as the pattern exists. Disordered patterns have been observed in several physical contexts, such as fingerprints [13], magnetic fluids [15], chemical reactions [16], fluid convection [17], vegetation [18], mussel beds [19], fish skin [20], Langmuir monolayers [21], and cholesteric liquid crystals [22], to name a few.

The nucleation, annihilation, dynamics, and characterization of the topological defects can play a relevant role in the emergence of different disordered patterns. Indeed, there are disordered patterns with a small or large number of defects. However, understanding these types of patterns, the role of their topological defects, and the transition between them is still an open question. In soft matter physics, chiral nematic liquid crystal cells provide a playground to study the emergence of disordered topological patterns in a controlled setting [23]. Disordered patterns in a chiral nematic liquid crystal cell are observed near the winding/unwinding transition. This transition occurs when the

* Corresponding author.
E-mail address: victor.fernandez.g@ug.uchile.cl (V. Fernandez-Gonzalez).

https://doi.org/10.1016/j.chaos.2024.114508
Received 14 December 2023; Accepted 20 January 2024
Available online 1 February 2024

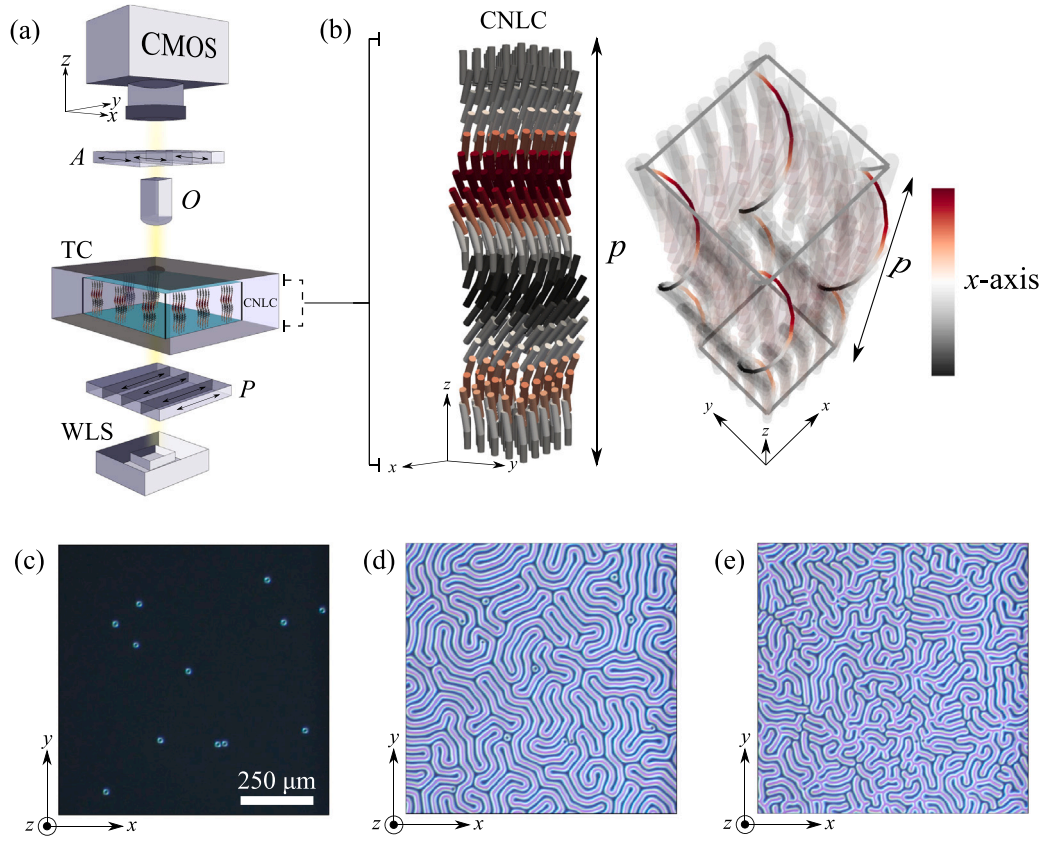

Fig. 1. Experimental observation of disordered patterns in a chiral nematic liquid crystal cell. (a) Schematic representation of the experimental setup. A chiral nematic liquid crystal (CNLC) cell is inside a thermal chamber (TC) and is being illuminated by a white light source (WLS). A, O, and P account for analyzer, objective, and polarizer, respectively. Both polarizers A and P are orthogonal. A complementary metal–oxide–semiconductor (CMOS) camera monitors the CNLC. The rods account for the CNLC. (b) Schematic representation of the CNLC helical structure, where p is the cholesteric pitch. The red and black colors represent the positive and negative sign of the projection of the director vector (average molecular orientation) on the x-axis, respectively. The colored curves follow the direction of the director vector along the pitch. (c) The unwind state of the CNLC cell observed state at 48 °C. The blue circles account for the glass bead spacers of the liquid crystal cell. (d) Invaginated and (e) branched patterns observed at 52 °C from the unwind state at 48 °C using a heating rate $\dot{T} = 0.02$ °C/min and $\dot{T} = 1.00$ °C/min, respectively. (For interpretation of the references to color in this figure legend, the reader is referred to the web version of this article.)

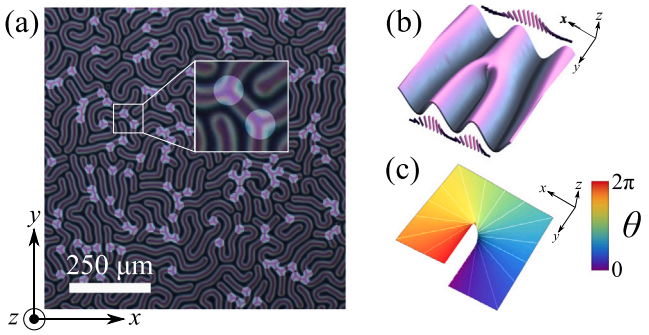

Fig. 2. Topological defects in disordered patterns. (a) Branching points in a disordered pattern observed at 52 °C from the unwind state at 48 °C using a heating rate $\dot{T} = 0.50$ °C/min. Inset accounts for an amplified region and the illuminated circles account for the pattern dislocation defects. (b) 3D representation of the dislocation of a pattern. The purple rods represent the vertical average director field at both ends of the dislocation. (c) Phase $\theta(x, y)$ of the pattern envelope. The phase jump indicates a topological singularity in the phase. (For interpretation of the references to color in this figure legend, the reader is referred to the web version of this article.)

helical structure of a chiral nematic liquid crystal develops/frustrates under the geometrical constraints imposed by molecular anchoring, *homeotropic configuration* [23,24].

Here, we investigate the formation mechanisms, defect emergence, and topological transition between disordered patterns driven by the heating rate. Based on a thermally driven chiral nematic liquid crystal experiment, we distinguish two disordered patterns, invaginated and branched. These patterns are obtained at the same temperature from the same initial state but at different heating rates. Namely, both disordered patterns coexist at the same temperature. Invaginated patterns have a small number of topological defects, contrary to what is observed in branched patterns, see Fig. 1(d) and (e). In fact, the local self-organization of defects differs between disordered patterns. The observed textures result from the different growth mechanisms of the cholesteric fingers emerging from the spacers and the homeotropic (unwound) state. Unexpectedly, by measuring the density of local defects, we characterize that the transition between these two disordered patterns is supercritical as a function of the heating rate. That is, the equilibrium depends on how the system is brought to it. Similarly, the correlation length obtained from the pair correlation function suggests a transition between the different disordered patterns. Theoretically, close to the winding/unwinding transition, the system is described by an amplitude equation with a chiral term. This model shows invaginated and branched disordered patterns as equilibria. In addition, the amplitude equation exhibits a supercritical transition between the different patterns in agreement with the experimental observations. Finally, we show that a prototype model of pattern formation exhibits a similar transition of disordered patterns, suggesting the universality of the phenomenon found.

2. Experiments and results

2.1. Experimental setup

A polarized optical microscope (POM, Leica DM2700P) was used to study the chiral nematic liquid crystal on a cell placed inside a thermal control microscopy stage (TC, Mod. LTS350E c/4 Elect LINKAM), which allows the temperature of the liquid crystal to be controlled. Fig. 1(a) shows a schematic of our experimental setup. The configuration has a white light source (WLS) that passes through a polarizer P and illuminates the liquid crystal sample. The objective O captures the transmitted light, which then reaches an analyzer A that is cross-polarized with respect to P. A complementary metal–oxide–semiconductor (CMOS) camera captures the transmitted light. The liquid crystal cell has homeotropic anchoring, which frustrates the helical structure of the CNLC. The degree of frustration across the mesophase is quantified by the confinement parameter $C = d/p$, where d and p are the cell thickness and the cholesteric pitch, respectively [23]. The pitch accounts for the characteristic rotational length of the molecules (see Fig. 1(b)) and depends on the temperature and the concentration of chiral molecules. The chiral nematic liquid crystal used in this experiment has E7 (Merck) as the nematic host and EOS-12 as the chiral molecule [25]. The winding/unwinding transition study was performed on a $d = 9$ μm cell containing a CNLC sample with a chiral dopant concentration of 7 wt % ($p = 13.2$ μm, at 50 °C). The pitch length is determined by the Grandjean-Cano technique [23].

2.2. Experimental transition between disordered patterns

Let us consider a chiral nematic liquid crystal sample, which is heated inside a thermal chamber (TC) and monitored by a polarized optical microscope; see a schematic representation of the setup in Fig. 1. The sample is heated to a temperature of 48 °C, which is below the cholesteric finger nucleation point. At this temperature, the winding state is stable (cf. Fig. 1(c)). The target temperature is set at 52 °C, which lies above the winding/unwinding transition point of the sample and is transited at different temperature heating rates $\dot{T}$. Once the system reaches the set temperature, the disordered pattern after transients remains stationary as the sample reaches equilibrium. To achieve different disordered patterns, we consider heating rates ranging from 0.10 °C/min to 0.90 °C/min with a step of 0.04 °C/min. The heating rate allows the system to access a higher or lower energy input, so it is possible to observe different equilibria, as the heating rate influences the dynamics of the cholesteric finger (see Fig. 3).

Due to the slow heating rate of the liquid crystal sample, nucleation of cholesteric fingers is observed. These cholesteric fingers originate from the spacers (glass beads) and imperfections in the system [22] (see Fig. 1(c)). These fingers start to elongate in a straight line with slow growth and suffer transversal modulation instabilities when they are large enough (see Fig. 3(a) and (g)); this dynamic has been termed wiggle dynamics [23,26]. Namely, the central part of the finger suffers spatial instability and begins to undulate. When the undulations have a sufficiently large amplitude, they suffer secondary transverse instabilities, and the process continues successively. Note that the fingers do not connect with each other (see Video 1 in Supplementary Materials [27]). Eventually, a stable invaginated pattern covers the system. Fig. 3(a) illustrates the process of formation of the invaginated pattern (see Video 1 in Supplementary Materials [27]). The previous scenario changes radically when fast heating rates are considered. Again, cholesteric fingers emerge in the system, but they elongate rapidly, and their tips and folds swell and generate two new tips [28], *branching process* (see Fig. 3(b) and (h)). This process is repeated for each new finger, ending with a stable branching pattern that covers the system. Fig. 3(b) shows the process of branching pattern emergence (cf. Video 1 in Supplementary Materials [27]). The difference in the behavior of the cholesteric fingers is because the heating rate allows a slower or faster ordering of the molecular orientation, which in turn is responsible for the collective self-organization of the pattern (see Fig. 3). To characterize the emergence, evolution, and saturation of the invaginated and branched patterns, we plotted the evolution of the cholesteric domain area over the homeotropic one (see Fig. 3(c) and (d)). One of the main differences between invaginated and branched patterns is the number of branching points. Dislocations correspond to the position where two new fingers emerge from one finger (see Fig. 2(b)). Therefore, the topological features and distributions of each disordered pattern are different. In the case of invaginated patterns, the defects result from side-branching, spacers, or experimental imperfections, while in branched patterns, the dominant process is tip-splitting. In this context, topological defects persist as long as the pattern does, as they are regarded as singularities of the pattern envelope. This scenario is similar to crystalline materials, where crystal dislocations are upheld as long as the crystal structure is not destroyed. An analogous topological transition is observed if one plastically bends a beam formed by a single crystal, thus inducing crystal dislocations along the crystal lattice [29]. We have experimentally measured the number of dislocations per unit area $\mathcal{N}$ as a function of the heating rate $\dot{T}$. Fig. 4(a) summarizes the results obtained.

This chart shows a systematic and continuous increase in the number of topological defects. Thus, the observed transition is supercritical in nature. To characterize the transition, we use the curve that describes a noisy or imperfect supercritical transition [30]

$$\mathcal{N}(\dot{T}) = C\sqrt{\frac{(\dot{T}-\dot{T}_c)+\sqrt{(\dot{T}-\dot{T}_c)^2+\eta}}{2}} + N_0, \tag{1}$$

where $\dot{T}_c$ is the deterministic transition critical heating rate, N_0 accounts for the defect density at low heating rates, which is determined by the imperfections of the system. η stands for the level of imperfection and noise of the system. C is a constant with suitable dimensions that connects the density of defects with heating rates. Note that for significant heating rates, the system grows with a square root law, $\mathcal{N} \propto \sqrt{\dot{T}-\dot{T}_c}$. Employing the formula (1), the transition of the system is well described, finding the critical heating rate $\dot{T}_c = 0.22 \pm 0.005$ °C/min by measuring the associated deterministic curve and considering the instrumental error. Then for $\dot{T} > \dot{T}_c$ ($\dot{T} < \dot{T}_c$), the system presents branched (invaginated) patterns. Likewise, based on the pair correlation function, we have determined the correlation length ξ as a function of heating rates (see Fig. 4(b)) [31]. This correlation length ξ is commonly used to determine transitions between different states of the matter by presenting a maximum or a minimum as a function of the bifurcation parameter [31]. That is, the qualitative change of the order in the system manifests itself in a change of the behavior of the correlation length in its growth or decrease. Thus, elucidating in this case, the emergence of topological defects in the chiral nematic cell. The correlation length ξ suggests a transition between the different disordered patterns. Note that the characteristic length of the disorder pattern λ depends on the heating rate, as summarized in Fig. 4(e). From this chart, it can be concluded that as the heating rate increases, the length of the pattern decreases.

2.3. Theoretical description

To shed light on the experimental observation, let us consider the system close to the winding/unwinding transition and in the long-pitch limit $p \gg l$, where l is a typical molecular length. The average molecular orientation is described by the director $\vec{n} \approx [\cos(z/p + \theta)\alpha \sin(\pi z/d), \sin(z/p + \theta)\alpha \sin(\pi z/d), 1]$, where $\alpha = \alpha(x, y, t)$ is an small tilt angle of $\vec{n}$ from the vertical z-axis, $\theta = \theta(x, y, t)$ is the azimuth angle of the director, and d is the thickness of the liquid crystal cell. x and y are the spatial coordinates and t is time. The dynamics of the director is characterized by minimizing the Frank-Oseen free energy [23]. Considering the director equation, the previous director

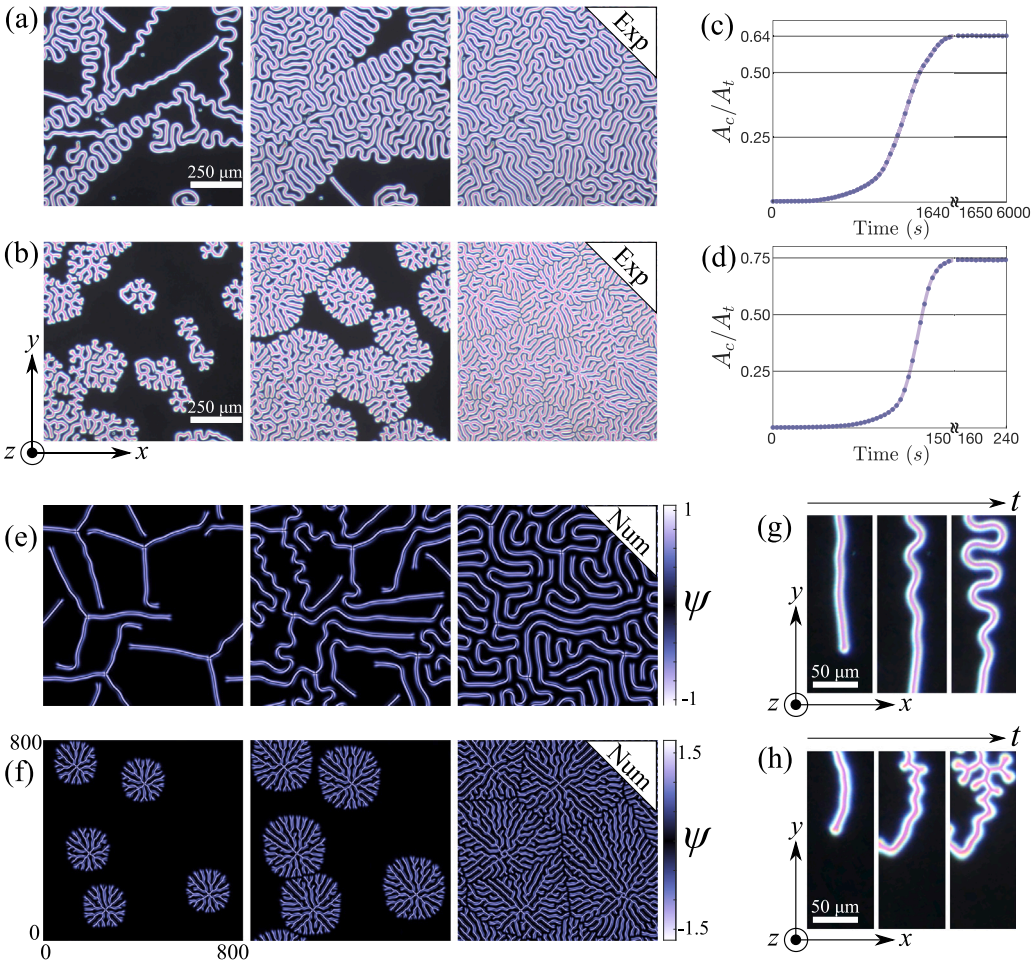

Fig. 3. Disordered patterns in chiral nematic liquid crystal cells. (a) and (b) Temporal evolution of cholesteric patterns at different heating rates. Top snapshots of the invaginated pattern formation heating at $\dot{T} = 0.04$ °C/min 25% left, 50% middle, and the equilibrium pattern 64% right panel of the observed cholesteric domain area A_c over the region A_t. Bottom snapshots of the branched pattern formation heating at $\dot{T} = 1.00$ °C/min 25% left, 50% middle, and the equilibrium pattern 75% right panel of the cholesteric versus homeotropic area. (c) and (d) Cholesteric proportion domain area versus time curve at heating rate $\dot{T} = 0.04$ °C/min and $\dot{T} = 1.00$ °C/min, respectively. (e) and (f) Temporal evolution sequence of the polarization field colormap $\psi = Re(A)Im(A)$ for numerical simulations of the amplitude Eq. (2) invaginated ($\gamma = 1$, $\mu = -0.6$, $\beta = 1$, $\delta = 0.07$, and $\chi = 3.05$) and branched regime ($\gamma = 1$, $\mu = -0.3, \beta = 1$, $\delta = 0.07$, and $\chi = 4$). Panels from left to right correspond to 15%, 30%, and 47% in (e) and 15%, 30%, and 70% in (f) of the cholesteric versus homeotropic state area. (g) and (h) Time sequence of snapshots that account for the destabilization of a cholesteric finger for an invaginated and branched pattern, respectively.

ansatz, and introducing the complex order parameter $A \equiv \alpha e^{i\theta}$, after straightforward calculations, we get (dimensionless chiral-anisotropic Ginzburg–Landau amplitude equation [32])

$$\gamma \partial_t A = \mu A + \beta A|A|^2 - A|A|^4 + \partial_{\eta\bar{\eta}} A + \delta \partial_{\eta\eta} \bar{A} + \chi \left(A \partial_{\bar{\eta}} A - \bar{A} \partial_{\eta} A \right), \qquad (2)$$

where γ is the rotational viscosity, μ accounts for the winding/unwinding control parameter, which is proportional to the confinement parameter $C = d/p$ minus the quotient of the bend elastic constant over twice the twist elastic constant (see Ref. [23] on page 467). β, δ, and χ are functions of the elastic constants and confinement parameter. $\partial_\eta = \partial_x + i\partial_y$ is a differential operator on the complex plane, the *Wirtinger derivative*. A derivation of the model (2) from first principles is given in [24]. The amplitude Eq. (2) has been used to understand chiral bubbles, fingers, and disordered patterns in cholesteric liquid crystals [23,24,32]. In particular, it is possible to use spherulites as nucleation sites capable of creating cholesteric fingers in the amplitude equation, which grow and form a disordered pattern as a function of the considered parameter region, which in similarity with the experimental observations, exhibits the emergence of dislocations (see Fig. 5). Fig. 3(e) and (f) show the emergent and stationary invaginated and branched patterns obtained in numerical integrations of model Eq. (2), respectively.

The elastic constants, rotational viscosity, and pitch are functions of temperature [23]. In the case of non-Newtonian fluids, the viscosity is a function of the heating rate [33,34]. However, the dependence of the parameters of model (2) as a function of heating rate is unknown. Nonetheless, the characteristic length of the pattern is shorter as the heating rate increases (see Fig. 4(e)). In addition, the chirality parameter χ controls the characteristic length of the patterns λ in Eq. (2) [24,32]. Hence, we use the chirality χ as the control parameter for the transition, as it controls the two-dimensional chiral effects on the model [24]. Fig. 4(c) and (d) show how the topological defect density $\mathcal{N}$ and the correlation length ξ vary as a function of chirality χ. Consequently, the amplitude Eq. (2) shows a supercritical transition between invaginated and branched patterns as a function of chirality χ. Following the same strategy used for the experimental analysis of the defect density $\mathcal{N}$, we use the equivalent formula (1) for the numerical results and find an excellent fit (see Fig. 4(c)). The fitted curve allows us to determine the critical chirality $\chi_c = 1.948$ and to establish the law

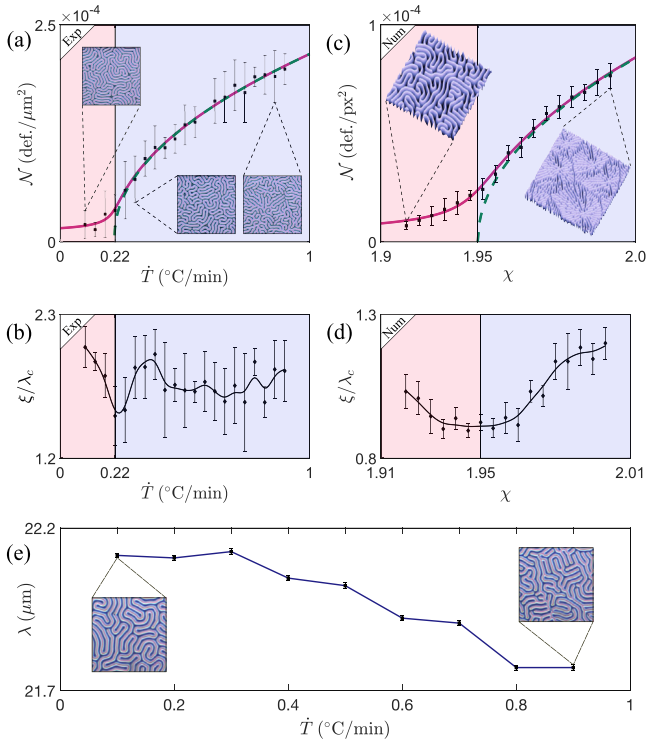

Fig. 4. Topological transition between disordered patterns. (a) Experimental supercritical bifurcation of the defects density $\mathcal{N}$ as a function of the heating rate $\dot{T}$. The points and error bar account for the mean value and standard deviation of $\mathcal{N}$, respectively. The supercritical transition (solid magenta line) is obtained using formula (1) with $C = 7589$, $\dot{T}_c = 0.22$, $\eta = 6\times10^{-4}$, and $N_0 = 2.807$. The deterministic curve (green segmented line) is plotted $\mathcal{N} = C(\dot{T} - \dot{T}_c)^{0.5}$. The critical heating rate $\dot{T}_c$ divides the invaginated (red color) and branched region (blue color). Insets showcase disordered patterns in different regions. (b) and (d) Experimental and numerical correlation lengths ξ as a function of the heating rate and chirality, respectively. The points and error bar account for the mean value and standard deviation of ξ. (c) Numerical supercritical bifurcation of $\mathcal{N}$ as a function of the chirality parameter χ obtained by integrating Eq. (2) with $\mu = -0.3$, $\beta = 1$, and $\delta = 0.07$. The magenta solid line is obtained using the appropriated formula (1) with $C = 4.8\times10^4$, $\chi_c = 1.948$, $\eta = 2\times10^5$, and $N_0 = 2.7\times10^{-8}$. The green segmented line represents the deterministic curve. The colored region stands for the different disordered patterns. Insets display a 3D representation of the typical amplitude $|A|$ for different regions. (e) λ as a function of the heating rate. From the 2D Fourier transform radial profile, the characteristic length was determined by considering a Gaussian fit at the dominant peak and measuring the distance to its mean. The insets show an amplified region of the pattern and have the same scale. The error bars account for the standard error of the measurement. (For interpretation of the references to color in this figure legend, the reader is referred to the web version of this article.)

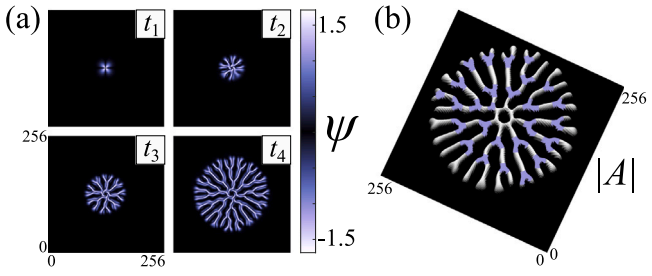

Fig. 5. Dislocation emergence in the numerical model. (a) Sequence of the polarization field $\psi = Re(A)\,Im(A)$ evolution over for numerical simulations of the amplitude Eq. (2) in the branched regime ($\gamma = 1$, $\mu = -0.3$, $\beta = 1$, $\delta = 0.1$, and $\chi = 3$). Temporal evolution of a spherulite as the initial condition for the finger nucleation with time, $t_1 < t_2 < t_3 < t_4$. (b) 3D representation of the typical amplitude $|A|$. The dislocations of the disordered pattern are highlighted in purple color. (For interpretation of the references to color in this figure legend, the reader is referred to the web version of this article.)

$\mathcal{N} \propto \sqrt{\chi - \chi_c}$. The correlation length also confirms this transition (see Fig. 4(d)).

2.4. Universal behavior

As we have mentioned, disordered patterns have been observed in various physical systems that exhibit pattern formation. Hence, the topological transition observed in chiral nematic liquid crystals could also be observed in other physical contexts. To shed light on this direction, let us consider the prototype scalar model of pattern formation (dimensionless non-variational Swift–Hohenberg model [35,36])

$$\partial_t u = \eta + \epsilon u - u^3 - \nu\nabla^2 u - \nabla^4 u + c(\nabla u)^2 + bu\nabla^2 u, \tag{3}$$

where $u(x, y, t)$ is a scalar order parameter. Depending on the physical context in which this model was derived, the physical meaning of u could be the electric field, molecular orientation deviation, phytomass density, chemical concentration, or elastic displacement, to name a few. η and ϵ are the bifurcation parameters that characterize the bistability region. $\nu < 0$ ($\nu > 0$) accounts for diffusion (anti-diffusion), and the terms proportional to b and c represent nonlinear diffusion and drift, respectively. Eq. (3) is a well-known paradigmatic model for studying spatially periodic and localized patterns. It has been derived for this purpose in liquid crystal light valves with optical feedback [35,36], in vertical cavity surface emitting lasers [37], in acoustic resonators containing viscous media [38], and in other fields of nonlinear science ranging from biological and chemical systems to physics [39]. The model Eq. (3) shows invaginated patterns when the localized spots are unstable [40]. Fig. 6(a) shows the time evolution of an unstable spot that causes an invaginated pattern to emerge. By modifying the parameters, a branching process is observed from a localized perturbation. Fig. 6(b) shows the temporal evolution of a perturbed spot that gives rise to a branched pattern. The observed topological transition between patterns is supercritical and is well described by formula (1) (see Fig. 6(c)). Recovering the result of the chiral nematic cell in Eq. (3) suggests that the observed transition is universal.

3. Conclusion

In this study, we characterize the equilibrium topological transition of disordered patterns in a chiral nematic liquid crystal cell subjected to thermal driving and varying temperature rates. Our results, which quantify the topological defect density in patterns, indicate a supercritical transition between the different equilibria. Theoretically, based on an amplitude equation with a chiral term valid near the winding/unwinding transition, similar phenomena are observed as a function of chirality, in good agreement with experimental observations. These results show that the chiral-anisotropic Ginzburg–Landau equation provides a solid framework for studying and understanding phenomena in the case of chiral nematic liquid crystals. Furthermore, the inherent process-dependent nature of the topological transition is considered. We have shown that the number of topological features in the system can depend on the process by which it is brought into equilibrium rather than fixing different energy levels. This result allows us to study novel phenomena in the self-organization of topological defects in equilibrium without the need for an increased energy input. In addition, an examination of a prototype pattern formation model reveals a similar transition, suggesting that topological transitions of this nature may exist in various disciplines, including physics, optics, biology, chemistry, and materials science. It is then plausible that pattern formation experiments may show similar behavior. In summary, we have studied the topological transition between disordered patterns by measuring the defect density of the final equilibria. Furthermore, we have shown that the transition observed in the chiral nematic liquid crystal cell is universal, using a prototype model of pattern formation. Comprehending the transition between different disordered patterns

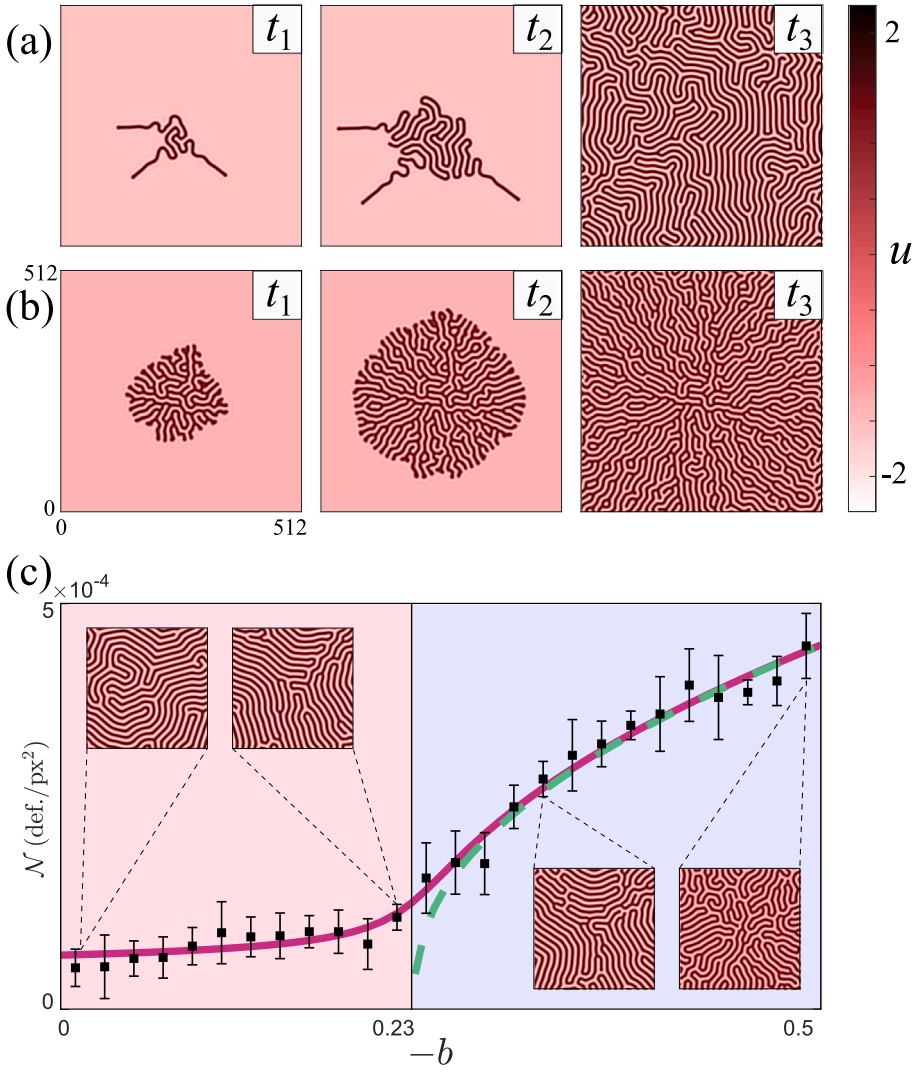

Fig. 6. Universal topological transition in pattern formation. Colormap of the invaginated and branched patterns obtained from the scalar Eq. (3) numerical simulation for (a) $\eta = -0.065$, $\epsilon = 2.45$, $\nu = 2$, $c = 0.01$, and $b = 0$ and (b) $\eta = -0.01$, $\epsilon = 1.29$, $\nu = 2$, $c = 0$, and $b = -0.26$. Temporal evolution of a perturbed spot with time, $t_1 < t_2 < t_3$. (c) Numerical supercritical bifurcation of the defects density $\mathcal{N}$ for Eq. (3) with $\eta = -0.1$, $\epsilon = 1$, $\nu = 2$, $c = 0.01$, and b was used as the bifurcation parameter. The error bar considers three realizations for different perturbed spots. The insets show an amplified region of the disordered patterns for different parameters. (For interpretation of the references to color in this figure legend, the reader is referred to the web version of this article.)

can also be useful for designing new materials, such as curvature-controlled wrinkling in the case of elastic spherical surfaces, which can be beneficial for further understanding tissue mechanics [41]. The study of phases with rich topological features, as well as the possibility to tune them, is crucial for the development of innovative materials. Our results pave the way for the creation of novel self-organized metasurfaces and metamaterials by taking advantage of how the system is brought to its equilibrium.

CRediT authorship contribution statement

Victor Fernandez-Gonzalez: Data curation, Formal analysis, Investigation, Methodology, Software, Visualization, Writing – review & editing. **Sebastián Echeverría-Alar:** Data curation, Formal analysis, Investigation, Methodology, Software, Writing – review & editing. **Jorge Vergara:** Resources, Writing – review & editing. **Paulina I. Hidalgo:** Conceptualization, Resources, Writing – review & editing. **Marcel G. Clerc:** Conceptualization, Funding acquisition, Investigation, Project administration, Resources, Supervision, Validation, Writing – original draft, Writing – review & editing.

Declaration of competing interest

The authors declare that they have no known competing financial interests or personal relationships that could have appeared to influence the work reported in this paper.

Data availability

Data will be made available on request.

Acknowledgments

V.F.-G., S.E.-A., and M.G.C. thanks the financial support of ANID-Millennium Science Initiative Program-ICN17_012 (MIRO) and FONDECYT, Chile Project No. 1210353. S.E.-A. acknowledges the financial support from ANID by Beca Doctorado Nacional, Chile 2020-21201376.

Appendix A. Correlation length

The correlation length ξ of the invaginated and branched patterns is computed from the pair correlation function of an orientational field

$\varphi(\vec{r})$, where $\vec{r}$ are 2D spatial coordinates. This function accounts for the local orientation of the cholesteric fingers and is obtained by locally approximating the cholesteric textures as stripe-like patterns [42].

The pair correlation function of the orientational field is $C_2(|\vec{r}-\vec{r'}|) = \langle\varphi(\vec{r})\varphi(\vec{r'})\rangle$, where the symbol $\langle\rangle$ corresponds to a spatial average process. Numerically, C_2 is obtained using the Correlation Theorem and Fast Fourier Transform algorithms [43]. The cholesteric patterns exhibit a decaying pair correlation function from which a correlation length ξ can be extracted. The limiting size of the simulation boxes motivates the extraction of the correlation length as the half width at half height of C_2 instead of fitting an exponential function [44].

Appendix B. Liquid crystal synthesis

EOS-12 is a phenyl ester group containing a chiral carboxylic part and a phenolic portion with a thiododecyl chain-substituted oxadiazole heterocycle. EOS-12 was synthesized, starting with a nucleophilic acyl substitution reaction of methyl 4-hidroxybenzoate with hydrazine and ethanol as a solvent. In this reaction, 4-hydroxybenzoic hydrazide is obtained. Treatment of this compound with carbon disulfide in the presence of potassium hydroxide yielded the 5-(4-hydroxyphenyl)-1,3,4-oxadiazoline-2-thione. The selective S-alkylation with dodecyl bromide of thione leads to the phenolic oxadiazole. Otherwise, the carboxylic group contains the chiral unit derived from (R)-2-octanol. The synthesis of the chiral benzoic acid was achieved by the Mitsunobu reaction starting from methyl 4-hydroxybenzoate and the chiral alcohol. It is known that this S_N2 reaction proceeded with an inversion of the configuration at the chiral center. The resulting ester was saponified, leading to the formation of chiral acid, followed by a reaction with oxalyl chloride. Finally, the optically active 4-(5-n-dodecylthio-1,3,4-oxadiazole- 2-yl)phenyl 4-(1″-methylheptyloxy)benzoate was obtained by esterification of the precursors aforementioned. The crude product was purified by column in Aluminum oxide 90 active basic (0.063–0.200 mm) in dichloromethane and circular chromatography (Chromatotron: dichloromethane/ethyl acetate 10/2) yielding 78% of a white solid $[\alpha]$D (ca. 0.0104 g/ml) = +38.5°. The mixtures E7/EOS-12 were prepared by weighing each component and dissolving them separately into dichloromethane. The solutions were combined and homogenized, sonicating for 5 min. The solvent was removed by slow evaporation at room temperature.

The organic solvents were of analytical grade quality and all were dried by traditional methods. Analytical thin layer chromatography (TLC) was conducted on Merck aluminum plates with 0.2 mm of silica gel 60 F-254. The structures of the compounds were confirmed by ^{1}H NMR and ^{13}C NMR (Bruker Ascend 400 MHz spectrometer) spectra and FTIR (Nicolet 550) spectra; the purity of the final products was evaluated by thin layer chromatography. Mesophases analysis was performed using an Olympus BX41 optical microscope equipped with an Olympus U-TV0.5XC-3 polarizer and a Linkam THMS600 heat stage and a RTVQIMAGING digital camera. The transition temperatures and enthalpies were investigated by DSC using a NETZSCH DSC 204 F1 Phoenix calorimeter. Samples were encapsulated in aluminum pans and studied at a scanning rate of 5 °C/min during heating and cooling. The instrument was calibrated using an indium standard (156.6 °C, 28.44 J/g). Optical rotational measurements were obtained using a Polax-2L automatic polarimeter. The samples were prepared in spectroscopy grade chloroform, and results are quoted at 25 °C with a monochromatic sodium light source.

Appendix C. Supplementary data

Supplementary material related to this article can be found online at https://doi.org/10.1016/j.chaos.2024.114508.

References

[1] Pethick CJ, Smith H. Bose–Einstein condensation in dilute gases. 2nd ed.. Cambridge University Press; 2008.
[2] Tsuneto T. Superconductivity and superfluidity. Cambridge University Press; 1998.
[3] Mühlbauer S, Binz B, Jonietz F, Pfleiderer C, Rosch A, Neubauer A, Georgii R, Böni P. Skyrmion Lattice in a chiral magnet. Science 2009;323(5916):915–9.
[4] de Gennes P, Prost J. The physics of liquid crystals. International series of monographs on physics, Clarendon Press; 1993.
[5] Pieranski P, Dubois-Violette E, Guyon E. Heat convection in liquid crystals heated from above. Phys Rev Lett 1973;30:736–9.
[6] Clerc MG, Kowalczyk M, Zambra V. Topological transitions in an oscillatory driven liquid crystal cell. Sci Rep 2020;10:19324.
[7] Nicolis G, Prigogine I. Self-organization in nonequilibrium systems. John Wiley & Sons; 1977.
[8] Murray J. Mathematical biology. Biomathematics, Springer Berlin Heidelberg; 2013.
[9] Turing AM. The chemical basis of morphogenesis. Philos Trans R Soc Lond Ser B Biol Sci 1952;237(641):37–72.
[10] Kleman M, Laverntovich O. Soft matter physics: an introduction. Partially ordered systems, Springer; 2003.
[11] Newell AC, Pomeau Y. Turbulent crystals in macroscopic systems. J Phys A: Math Gen 1993;26(8):L429.
[12] Pismen L. Patterns and interfaces in dissipative dynamics. Springer New York; 2009.
[13] Kücken M, Newell AC. Fingerprint formation. J Theoret Biol 2005;235(1):71–83.
[14] Cross M, Greenside H. Pattern formation and dynamics in nonequilibrium systems. Cambridge University Press; 2009.
[15] Rosensweig RE, Zahn M, Shumovich R. Labyrinthine instability in magnetic and dielectric fluids. J Magn Magn Mater 1983;39(1):127–32.
[16] Lee KJ, McCormick WD, Ouyang Q, Swinney HL. Pattern formation by interacting chemical fronts. Science 1993;261(5118):192–4.
[17] Morris SW, Bodenschatz E, Cannell DS, Ahlers G. Spiral defect chaos in large aspect ratio Rayleigh-Bénard convection. Phys Rev Lett 1993;71:2026–9.
[18] von Hardenberg J, Meron E, Shachak M, Zarmi Y. Diversity of Vegetation patterns and desertification. Phys Rev Lett 2001;87:198101.
[19] Liu Q-X, Herman PMJ, Mooij WM, Huisman J, Scheffer M, Olff H, van de Koppel J. Pattern formation at multiple spatial scales drives the resilience of mussel bed ecosystems. Nature Commun 2014;5(1):5234.
[20] Barrio RA, Varea C, Aragón JL, Maini PK. A two-dimensional numerical study of spatial pattern formation in interacting turing systems. Bull Math Biol 1999;61(3):483–505.
[21] Khattari Z, Fischer TM. Shapes of Langmuir monolayer domains in confined geometries. J Phys Chem B 2002;106(7):1677–83.
[22] Oswald P, Baudry J, Pirkl S. Static and dynamic properties of cholesteric fingers in electric field. Phys Rep 2000;337(1):67–96.
[23] Oswald P, Pieranski P. Nematic and cholesteric liquid crystals. CRC Press; 2005.
[24] Echeverría-Alar S, Clerc MG, Bordeu I. Emergence of disordered branching patterns in confined chiral nematic liquid crystals. Proc Natl Acad Sci 2023;120(15):e2221000120.
[25] Parra ML, Hidalgo PI, Elgueta EY. Synthesis and mesomorphic properties of oxadiazole esters derived from (R)-2-octanol, (S)-2-n-octyloxypropanol and (2S,3S)-2-chloro-3-methylpentanol. Liq Cryst 2008;35(7):823–32.
[26] Ribiere P, Oswald P. Nucleation and growth of cholesteric fingers under electric field. J Phys Fr 1990;51(16):1703–20.
[27] See Supplemental Material videos showing the emergence and formation of disordered patterns in a chiral nematic liquid crystal cell.
[28] Nagaya T, Hikita Y, Orihara H, Ishibashi Y. Experimental study of the growth of the cholesteric finger pattern. J Phys Soc Japan 1996;65(8):2707–12.
[29] Nabarro F. Theory of crystal dislocations. International series of monographs on physics, Clarendon P.; 1967.
[30] Agez G, Clerc MG, Louvergneaux E. Universal shape law of stochastic supercritical bifurcations: Theory and experiments. Phys Rev E 2008;77:026218.
[31] Egolf DA, Greenside HS. Characterization of the transition from defect to phase turbulence. Phys Rev Lett 1995;74:1751–4.
[32] Clerc MG, González-Cortés G, Echeverría-Alar S. Localized dissipative vortices in chiral nematic liquid crystal cells. Phys Rev Res 2022;4:L022021.
[33] Bacon RF, Fanelli R. The viscosity of Sulfur1. J Am Chem Soc 1943;65(4):639–48.
[34] Bloksma AH. Effect of heating rate on viscosity of wheat flour doughs1. J Text Stud 1980;10(3):261–9.
[35] Clerc MG, Petrossian A, Residori S. Bouncing localized structures in a liquid-crystal light-valve experiment. Phys Rev E 2005;71:015205.
[36] Durniak C, Taki M, Tlidi M, Ramazza PL, Bortolozzo U, Kozyreff G. Modulated optical structures over a modulationally stable medium. Phys Rev E 2005;72:026607.

[37] Kozyreff G, Chapman SJ, Tlidi M. Interaction of two modulational instabilities in a semiconductor resonator. Phys Rev E 2003;68:015201.
[38] Pérez-Arjona I, Sánchez-Morcillo VJ, de Valcárcel GJ. Ultrasonic cavity solitons. Europhys Lett 2008;82(1):10002.
[39] Kozyreff G, Tlidi M. Nonvariational real Swift-Hohenberg equation for biological, chemical, and optical systems. Chaos 2007;17(3):037103.
[40] Bordeu I, Clerc M, Lefever R, Tlidi M. From localized spots to the formation of invaginated labyrinthine structures in a Swift–Hohenberg model. Commun Nonlinear Sci Numer Simul 2015;29(1):482–7.
[41] Stoop N, Lagrange R, Terwagne D, Reis PM, Dunkel J. Curvature-induced symmetry breaking determines elastic surface patterns. Nature Mater 2015;14:337–42.
[42] Egolf DA, Melnikov IV, Bodenschatz E. Importance of local pattern properties in spiral defect chaos. Phys Rev Lett 1998;80:3228–31.
[43] Bracewell RN. The Fourier transform and its applications. McGraw-Hill; 1986.
[44] Cross MC, Meiron DI. Domain coarsening in systems far from equilibrium. Phys Rev Lett 1995;75:2152–5.